Experimental and Simulation Study of PEMFC based on Ammonia Decomposition Gas as Fuel

Jian Feng Zhao, Yi Fan Liang*, Qian Chaos Liang, Meng Jie Li, and Jin Yi Hu

College of Power Engineering, Naval University of Engineering, Wuhan, Hubei, 43003, China

ABSTRACT

Compared with hydrogen, ammonia has the advantages of high gravimetric hydrogen densities (17.8 wt.%), ease of storage and transportation as a chemical hydrogen storage medium, while its application in small-scale on-site hydrogen production scenarios is limited by the need for complex separation equipment during high purity hydrogen production. Therefore, the study of PEMFC, which can directly utilize ammonia decomposition gas, can greatly expand the application of fuel cells. In this paper, the output characteristics, fuel efficiency and the variation trend of hydrogen concentration and local current density in the anode channel of fuel cell with the output voltage of PEMFC fueled by ammonia decomposition gas were studied by experiment and simulation. The results indicate that the maximum output power of the hybrid fuel decreases by 9.6% compared with that of the pure hydrogen fuel at the same inlet hydrogen equivalent. When the molar concentration of hydrogen in the anode channel is less than 0.12, the output characteristics of PEMFC will be seriously affected. Employing ammonia decomposition gas as fuel, the efficiency corresponding to the maximum output power of PEMFC is approximately 47%, which is 10% lower than the maximum efficiency of pure hydrogen.

1. Introduction

In recent years, proton exchange membrane fuel cell (PEMFC) has obtained preliminary commercial application [1]. However, PEMFC still uses high purity hydrogen as fuel at present. Due to the high production cost of high purity hydrogen [2] and low volume energy density [3], the large-scale application of PEMFC is limited. Therefore, how to obtain hydrogen sources with high volume energy density and easy access on site is the primary problem for realizing the large-scale application of fuel cells [4-6]. Current potential solutions include hydrocarbon fuel reforming for hydrogen production, metal hydrogen storage, liquid organic hydrogen storage and inorganic compound hydrogen storage. CO which is harmful to the fuel cell, is an unavoidable by-product In the reforming process of hydrocarbon fuel and

therefore must be separated out. Meanwhile, carbon deposition in the reforming process is also a huge difficulty for hydrogen production from hydrocarbon fuel [7-9]. Secondly, both metal hydrogen storage and liquid organic hydrogen storage have lower hydrogen storage densities at present, and liquid organics produce harmful by-products in the process of hydrogen release [10-14]. Liquid ammonia is an ideal hydrogen carrier with prominent advantages such as high hydrogen storage density, easy transportation, low market price, and no carbon-containing gas in its decomposition products [15,16].

Due to the limitation of chemical equilibrium, there is residual ammonia in the ammonia decomposition gas, which leads to deterioration of PEMFC performance when the concentration of ammonia is greater than 2 ppm [17]. But the residual ammonia gas is easily absorbed and separated, including dissolution in water [18], reaction with phosphoric acid [19] to form ammonium phosphate $((NH_4)xH_{3-x}PO_4)$, adsorption by molecular sieve or activated carbon [20], and formation of complexes with metal halides [21]. At present, higher purity hydrogen can

*E-mail address: YFanLiang@yeah.net

be obtained by pressure swing adsorption, composite metal palladium membrane separation and other methods [22,23]. But for small portable PEMFC devices, these methods may seem too bulky. Therefore, the development of a PEMFC that directly utilizes ammonia decomposition gas (Referred as gas mixture in this paper) is of great interest and can greatly expand the application of PEMFC. The feasibility of ammonia as a fuel has been initially verified on a 100 W dead-ended PEMFC system by Hazel M.A. Hunter et al. [24].

In this paper, the output characteristics of PEMFC and the appropriate fuel supply strategy when ammonia decomposition gas as fuel are first studied through experiments and then a two-dimensional single-channel PEMFC model is established to further analyzes the effect of output voltage on the hydrogen concentration and local current density inside the PEMFC flow channel. Finally, a comparative analysis of the efficiency under different fuel supply scenarios was performed. The results can provide a reference for evaluating the feasibility of using ammonia decomposition gas as fuel for PEMFC.

2. Experimental

2.1. System description

Fig. 1 shows the schematic description of the whole system, which can be subdivided into two subsystems, the ammonia decomposition system and the PEMFC system, respectively. The ammonia decomposition system contains ammonia storage bottle, flow quantitative meter, electric heating and holding furnace, ammonia cracker (316 stainless steel tube, inner diameter 19 mm, length 900 mm, filled with NiO-Al$_2$O$_3$ catalyst, NiO>14 wt.%), ammonia purifier (Plexiglas tube, diameter 100 mm, length 600 mm, filled with saturated salt water), gas dehumidifier, -mass spectrometer. The working process of the system is as follows.

Firstly, the ammonia cracker is heated to 750°C by electric heating furnace keep the temperature constant. Secondly, the ammonia gas enters the ammonia cracker according to the flow rate set by the flow quantitative meter to generate the mixture gas, which is cooled to below 35°C by the heat exchanger, and then enters the purifier to remove the residual ammonia gas, and the purified mixture gas enters the gas mass spectrometer after passing the dehumidifier. When the detected residual amount of ammonia is less than 2 ppm, the mixure gas can be passed to the PEMFC system. If the residual ammonia is greater than 2 ppm, it should improve the working temperature of resolver.

The main components of the experimental system include two fuel flow controllers, three bypass valves, a commercial PEMFC stack (rated power 1 kW, 51 cells, with a single cell of 19 cm in length and 5 cm in width and an effective area of 90 cm^2 per cell) and a 2 kW electronic load. The operating mode of the experimental system can be flexibly changed by controlling the bypass valve and the flow control valve.

2.2 Experimental scheme

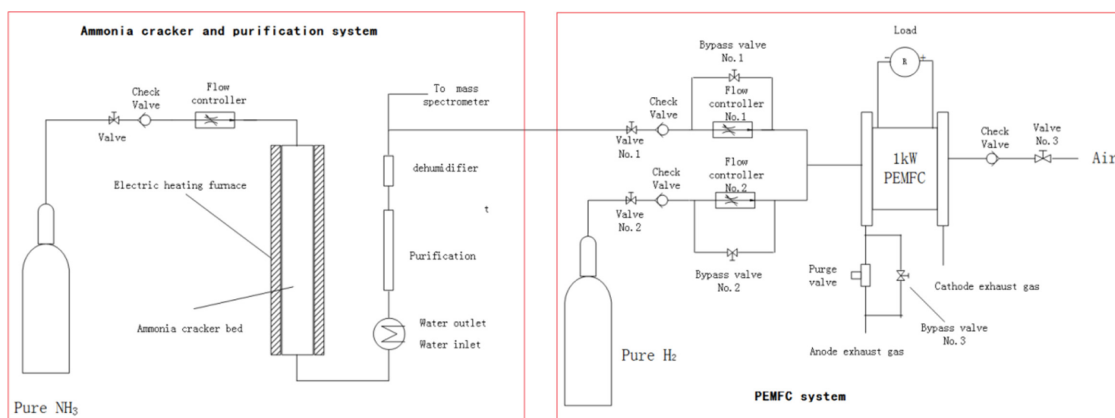Seven schemes were conducted according to the control method of fuel supply (constant flow rate,

Fig. 1. Schematic diagram of experimental system.

Table 1. Experimental scheme

Scheme	Fuel	Control mode of anode tail gas emission	Standard volume flow (L/min)
1	pure H_2	purge	----
2	pure H_2	open	10
3	mixture gas	open	10.5
4	mixture gas	open	12.0
5	mixture gas	open	13.5
6	mixture gas	open	15.0
7	mixture gas	purge	----

anode purge), fuel type (hydrogen, mixture gas) and flow rate of fuel, as shown in Table 1.

3. Mathematical modeling

In order to further analyze the variation trend of gas composition and electric field inside anode domain, a two-dimensional simulation model is established in this paper [22].The following assumptions were made with reference to literature [24-28].

(1) Each gas is regarded as an ideal gas.
(2) The generated water can quickly flow out with air in a gaseous form, and there is no liquid water in the cathode.
(3) The temperature distribution in PEMFC is uniform and constant.
(4) The penetration of water and nitrogen from the cathode side to the anode side is ignored.

Meanwhile, the PEMFC used in this paper relies on the air in the cathode channel for forced cooling, so the air flow rate inside the cathode is much larger than the amount of air required for the electrochemical reaction of the cell, and the width of a single anode channel is only 2 mm, so it can be assumed that the air composition on the outer surface of the cathode gas diffusion layer is the same as that at the air inlet [23].

The model contains six domains: anode channel, anode gas diffusion layer (an_GDL), anode catalyst layer (an_CL), proton exchange membrane (PEM), cathode catalyst layer (ca_CL), and cathode gas diffusion layer (ca_GDL) as shown in Fig. 2.

3.1. Electrochemical model

The cell voltage V is described as follows:

$$V = E_0 - \eta_{act} - \eta_{ohm} \tag{1}$$

Where E_0 is the theoretical reversible voltage which can be calculated from the Nernst equation[22]:

$$E_0 = 1.229 - 0.85*10^{-3}*(T-298.15) \tag{2}$$
$$+ 4.3085*10^{-5}*T*[In(P_{H_2}^*) + 0.5*In(P_{O_2}^*)]$$

Anode local current density i_a (Butler-Volmer equation)

$$i_a = i_{0,a}(\frac{c_{H_2}}{c_{H_2,ref}})(\exp(\frac{\alpha_{a,a}F\eta_a}{RT}) - \exp(\frac{-\alpha_{c,a}F\eta_a}{RT})) \tag{3}$$

Cathode local current density i_c (Butler-Volmer equation)

$$i_c = -i_{0,c}(\frac{c_{O_2}}{c_{O_2,ref}})(\exp(\frac{\alpha_{c,a}F\eta_c}{RT}) - \exp(\frac{-\alpha_{c,c}F\eta_c}{RT})) \tag{4}$$

F is the Faraday's constant (SI unit: C mol^{-1}), $c_{i,ref}$ is the material reference concentration (SI unit: mol m^{-3}), $i_{0,a}$ and $i_{0,c}$ is the standard exchange current density (SI unit: A m^{-2}), R is the gas constant, T is the temperature (SI unit: K), $\alpha_{a,a}$, $\alpha_{a,c}$, $\alpha_{c,a}$, $\alpha_{c,c}$ is the transfer coefficient.
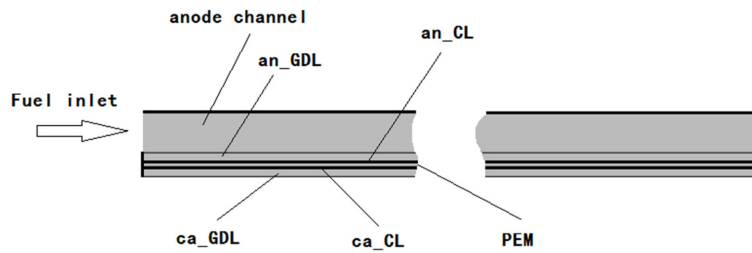
Fig. 2. Two-dimensional section of the modeling area.

Anode over-potential η_a, cathode over-potential η_c and total over-potential η_{act} are given by the following equation:

$$\eta_a = \phi_s - \phi_l - E_{eq,a} \tag{5}$$

$$\eta_c = \phi_s - \phi_l - E_{eq,c} \tag{6}$$

$$\eta_{act} = \eta_a + \eta_c \tag{7}$$

Where $E_{eq,i}$ (SI unit: V) represents the equilibrium voltage, φ_s is the electronic potential (IS unit: V), and φ_l is the ionic potential (IS unit: V).

The potential difference between the cathode and anode current collectors corresponds to the total cell voltage. Choose the potential at the upper surface of an_GDL as the reference level by setting it to zero. Then the total cell voltage serves as the boundary condition at the lower surface of ca_GDL:

$\phi_s = 0$ at the upper surface of an_GDL
$\phi_s = V$ at the lower surface of ca_GDL

Ohmic overpotentia η_{ohm}:

$$i_e = \sigma_e * \eta_{ohm,e} \tag{8}$$

Where σ_e (IS unit: S m^{-1}) is the electrical conductivity (where the index e stands for "a"(anode) or "c"(cathode)).

3.2. Momentum conservation equation

Navier-Stokes equation and Brinkman equation are adopted to describe the flow in the free zone (anode channel) and porous zone, respectively. [29] The combination of Navier-Stokes equations and continuity equations can be expressed as:

$$(\rho u \cdot \nabla)u = -\nabla P + \nabla \cdot [\mu(\nabla u + (\nabla u)^T) - \frac{2}{3}\mu(\nabla \cdot u)I] \tag{9}$$

$$\nabla \cdot (\rho u) = 0 \tag{10}$$

Where ρ is the mixture density of the gas phase (SI unit: kg m^{-3}), I is Unit Matrix, P is the pressure (SI unit: Pa), μ represents the gas viscosity (SI unit: Pa s), u is the velocity.

The combination of Brinkman equation and continuity equation can be expressed as:

$$\frac{\mu}{k}u = -\nabla p + \nabla \cdot \frac{1}{\varepsilon}[\mu(\nabla u + (\nabla u)^T) - \frac{2}{3}\mu(\nabla \cdot u)I] \tag{11}$$

Where k is permeability(IS unit: m^2), ε is porosity.

3.3. Mass conservation equation

The model takes into account two species in the anode (H_2 and N_2) and three at the cathode (O_2, H_2O and N_2), and uses Maxwell-Stefan multicomponent diffusion, governed by the following equations [29]:

$$\nabla j_i + \rho(u \cdot \nabla)w_i = R_i \tag{12}$$

Where w_i is mass fraction of species i, R_i is chemical reaction rate of species i(IS unit: kg m^{-3} s^{-1}), j_i is the diffusion mass flow density of species i, which is defined as follows:

$$j_i = -(\rho D_i^m \nabla w_i + \rho w_i D_i^m \frac{\nabla M_n}{M_n} - j_{c,i}) \tag{13}$$

$$D_i^m = \frac{1 - w_i}{\sum_{k \neq l} \frac{x_k}{D_{ik}}} \tag{14}$$

$$M_n = (\sum_i \frac{w_i}{M_i})^{-1} \tag{15}$$

$$j_{c,i} = \rho w_i \sum_i \frac{M_i}{M_n} D_k^m \nabla x_k \tag{16}$$

Here x_k is mole fraction, M_i is Molecular mass, D_i^m is the equivalent diffusion coefficient of species i in multicomponent, D_{ik} is binary diffusion coefficient, which can be calculated by Fuller's empirical formula [30]:

$$D_{ik} = 3.198 * 10^{-8} * \frac{T^{1.75}}{P(v_i^{\frac{1}{3}} + v_k^{\frac{1}{3}})^2}(\frac{1}{M_i} + \frac{1}{M_k})^{0.5} \tag{17}$$

Where v_i is the molar diffusion volume of gas (IS unit: cm^3 mol^{-1}).

The binary diffusion coefficient obtained by Equation (20) needs to be modified in the porous region:

$$D_{ik\_eff} = \frac{\varepsilon}{\tau}D_{ik} \tag{18}$$

Here τ is the tortuosity factor.

Inside the anode channel, an_GDL and ca_GDL domains:

$$R_i = 0 \tag{19}$$

Inside the an_CL and ca_CL domains:

$$R_i = -\frac{i_e}{nF}M_i \tag{20}$$

Here n = 2 when e = a, n = 4 when e = c.

3.4. Fuel efficiency
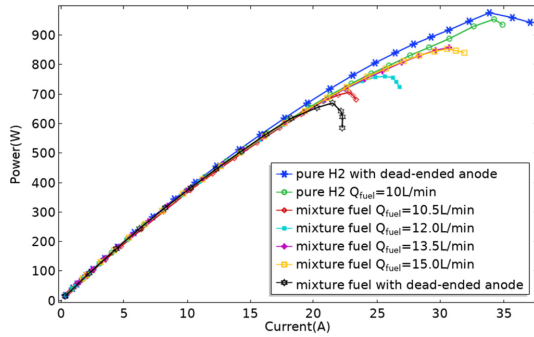
The fuel efficiency equation is set up as follows:

Fig. 3. Variation of power versus current in different cases.

Fig. 4. Variation of voltage versus current in different cases.

$$\varphi = \frac{W}{Q_{fuel} w_{H_2} H_{H_2}} \tag{21}$$

Here H_{H_2} is the low energy value of hydrogen per unit mass (IS unit: J kg⁻¹), W is the PEMFC's power (IS unit:W).

4. Results and Discussion

4.1. Experimental results and analysis

Fig. 3 shows the variation of output power versus current for different schemes. It can be seen that scheme 7 has the worst result performance, which indicates that the purge control method is not applicable to mixture gas, so scheme 7 is removed in the subsequent analysis. While using the flow control method, it can be seen from the result performance of schemes 3-6 that the maximum output power of the fuel cell no longer increases with the increase of fuel flow after rising to a peak value, which is 859 W. Scheme 1 has a peak power of 1010 W when using pure hydrogen fuel, so the maximum power of the mixture gas is 15% lower than that of the pure hydrogen. Scheme 2 has the same hydrogen equivalent flow rate as scheme 5, and the maximum output power of scheme 2 is 950 W. The maximum power of the mixture gas is 9.6% lower at the same hydrogen equivalent flow rate. Therefore, the use of mixture gas reduces the performance of PEMFC, and also reduces the output power at the same hydrogen equivalent flow rate.

Fig. 4 shows the variation of fuel cell output voltage versus current under different schemes. When the Mixture gas is used, the diffu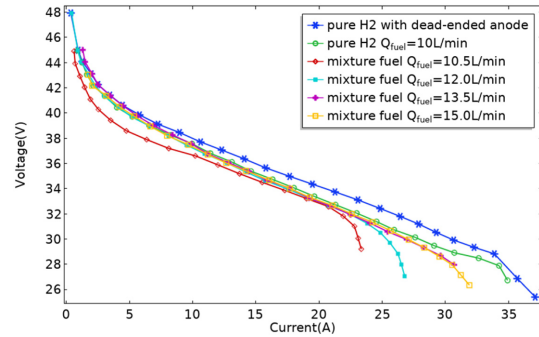sion of hydrogen from the mainstream airflow to the catalytic reaction section of the electrode is mainly affected by the partial pressure of hydrogen and the diffusion coefficient of hydrogen. Both of these two factors are affected by nitrogen. It can be seen from the figure that in the low current range, the output characteristics of the Mixture gas are basically the same as that of the pure hydrogen fuel. However, in the large current range, the difference gradually increases. This indicates that the change of hydrogen concentration has little effect on the output characteristics of the fuel cell at low current output. However, when approaching the maximum power output, the output characteristics of the fuel cell rapidly deteriorate due to the combined influence of the concentration difference and the hysteresis effect of nitrogen on hydrogen diffusion.

4.2. Verification of simulation model

Table 2 shows the geometric parameters, characteristic parameters and boundary conditions of the simulation model. The fuel inlet velocity was calculated with a volume flow rate of 13.5 L/min. Fig. 5 shows the comparison between simulation and Experimental results. The simulation values are in good agreement with the experimental values, and the maximum relative error is 4%. Increased error between experimental and simulated values in high current region (peak area corresponding to curve in figure), and the simulated value is larger. The reason is that the experimental value is the average value obtained based on the actual overall output characteristics of the fuel cell, so the average concentration of oxygen at the cathode side is less than the assumption in the simulation model at large current, so the simulation result is higher than the experimental value.

Table 2. Geometric parameters, characteristic parameters and boundary conditions of the model

Parameters	Value	Ref.
Anode channel length, L(mm)	180	measure data
Anode runner height, H(mm)	1	measure data
Anode gas diffusion layer thickness, σ_{ad}(mm)	0.29	[28]
Cathode gas diffusion layer thickness, σ_{cd}(mm)	0.254	[28]
Anode catalyst layer thickness, σ_{ac}(mm)	0.0165	[28]
Cathode catalyst layer thickness, σ_{cc}(mm)	0.0165	[28]
PEM thickness, σ_m(mm)	0.0508	[28]
Electrical conductivity, σ_s(S m^{-1})	220	[34]
Ionic conductivity, σ_l(S m^{-1})	5.2	[34] and Optimization
Permeability inside an_GDL and ca_GDL domains, κ_{dgl}(m^2)	1.18×10^{-11}	[34]
Permeability inside an_CL and ca_CL domains, κ_{cl}(m^2)	2.36×10^{-12}	[34]
Porosity inside an_GDL and ca_GDL domains, ε_{dgl}	0.4	[34]
Porosity inside an_CL and ca_CL domains, ε_{cl}	0.3	[34]
Gas viscosity inside anode domains, μ_a(Pa s)	1.19×10^{-5}	[27]
Gas viscosity inside cathode domains, μ_a(Pa s)	2.46×10^{-5}	[27]
Anode standard exchange current density, i_{0a}(A m^{-2})	1×10^5	[34] and Optimization
Cathode standard exchange current density, i_{0c}(A m^{-2})	1.0	[34] and Optimization
Transfer coefficient, $\alpha_{a,a}, \alpha_{a,c}, \alpha_{c,a}, \alpha_{c,c}$	1,1,1.26,0.74	[28] and Optimization
Tortuosity factor τ	1.4	[34]
Cell temperature, T(K)	318	measure data
Fuel inlet velocity, v_{fuel}(m/s)	0.184	measure data
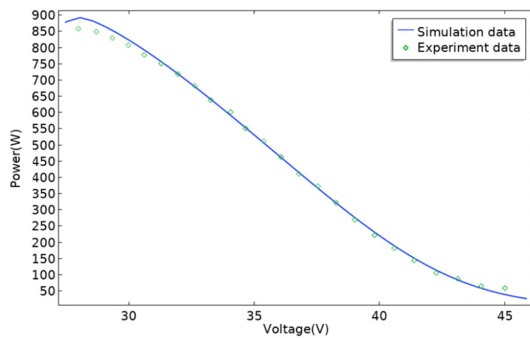
Fig. 5. Comparison of simulation values and experimental values.
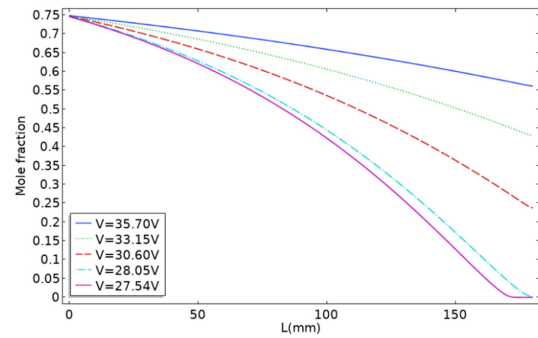
Fig. 6. The change curve of hydrogen molar concentration in anode channel at different output voltages.

4.3. Hydrogen concentration distribution

Fig. 6 shows the variation curves of hydrogen molar concentration inside the anode domain under different output voltages. Hydrogen concentration at the anode outlet shows a downward trend with voltage decreasing. When the output voltage is less than 28 V, the hydrogen concentration at the outlet of the anode is close to 0. And as the output voltage decreases further, the region where the hydrogen concentration is close to 0 develops from the outlet to the inside of the anode. To ensure the stable working per-

formance of the PEM, the concentration of hydrogen in the cell must not be too low, so the hydrogen concentration close to 0 needs to be avoided. At the same time, too low hydrogen concentration will in turn increase the polarization loss of the cell, which will reduce the output power of the cell and lead to a decrease in the efficiency of the fuel cell. Therefore, the minimum output voltage of the cell needs to be limited.

4.4. Current density analysis

Fig. 7 shows the current density distribution along the direction of fuel flow in the fuel cell under different output voltages. When the output voltage is high, the current density distribution along the direction of fuel flow is relatively uniform due to the high hydrogen concentration in the entire anode passage. With the decrease of output voltage, the hydrogen concentration at the anode outlet has more and more influ-
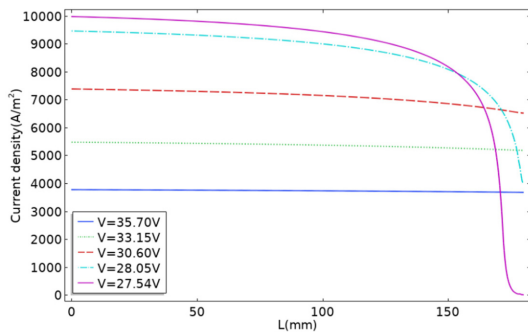
ence on the local current density. When the molar concentration of hydrogen is less than 0.12, the current density decreases rapidly. This will cause the rear membrane electrode to fail to work normally, reducing the utilization rate of the membrane electrode, and even cause the membrane electrode to work in reverse, from the battery state to the electrolytic cell state. Therefore, this phenomenon needs to be avoided.

4.5. Fuel efficiency

Fig. 8 shows the fuel efficiency curve calculated from the experimental data. It can be seen that the efficiency of using mixture gas is less than that of pure hydrogen, and when the equivalent flow rate of hydrogen is the same, the maximum efficiency of mixture gas (Scheme 5) is 47%, while the maximum efficiency of pure hydrogen is 52%, and the maximum efficiency of mixture gas is decreased by about 10% compared to the maximum efficiency of pure hydrogen. The Maximum efficiency increases with mixed gas flow rate decreasing, indicating that PEMFC can operate efficiently at low power levels by properly controlling the fuel supply.

Fig. 9 shows the maximum efficiency and corresponding output voltage of PEMFC under different output power obtained by model simulation. The efficiency curve shows that the efficiency of PEMFC increases with the decrease of power, which verifies the above conclusion. At the same time, it can also be seen from the figure that the voltage corresponding to the highest efficiency operating point also increases with the decrease of power.

Fig. 7. The change curve of current density in anode channel at different output voltages.
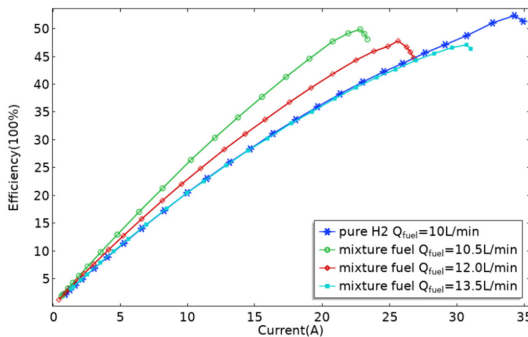
Fig. 8. Variation of fuel cell efficiency versus output voltage.
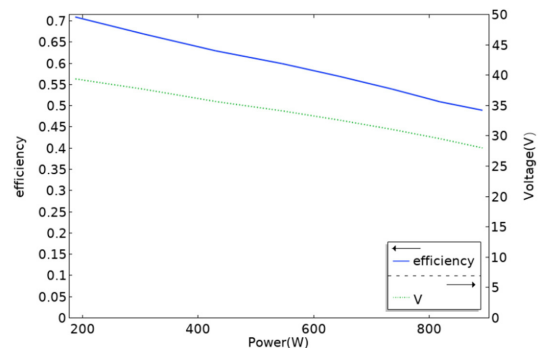

Fig. 9. Maximum efficiency and corresponding output voltage of PEMFC at different output power.

5. Conclusions

The PEMFC output characteristics are experimentally investigated in the case with mixture gas as fuel, and contrasted with pure hydrogen's. Mean-while, Based on this result, a single-channel two-dimensional model is established. Subsequently, exploring the variation trend of hydrogen concentration and local current density with output voltage inside the fuel cell. Ultimately analyzing PEMFC fuel efficiency. The following results were obtained.

1. the maximum output power of the mixture gas decreases by 9.6% compared with that of the pure hydrogen fuel with the same hydrogen equivalent.

2. The effect of nitrogen on the fuel cell output characteristics is mainly in the high current output stage, while the steady-state output characteristics of mixture gas and pure hydrogen are basically the same in the low current output stage.

3. The results show that the local current density drops sharply when the molar concentration of hydrogen is below 0.12. Therefore, the lowest output voltage of the fuel cell needs to be limited to avoid this phenomenon.

4. The maximum efficiency of the mixture gas is about 47%, which is 10% lower than the maximum efficiency of pure hydrogen.

5. When using mixture gas, the voltage value corresponding to the highest efficiency operating point of PEMFC increases with the decrease of power.

6. The anode purge control strategy is not applicable to mixture gas.

References

[1] Z. P. Cano, D. Banham, S. Ye, A. Hintennach, J. Lu, M. Fowler, *Nat. Energy*, **2018**, *3(4)*, 279-289.

[2] M. Khzouz, E. I. Gkanas, S. Jia, F. Sher, M. A. Qubeissi, *Energies*, **2020**, *13(15)*, 3783.

[3] R. Moradi, K. M. Groth, *Int. J. Hydrog. Energy*, **2019**, *44(23)*, 12254-12269.

[4] X. Wu , N. Li, X. Wang, W. Zhao. *IEEE Transactions on Sustainable Energy*, *12(2)*, 1020-1031.

[5] G. Yang, Y. Jiang, *Int. J. Energy Res.*, **2020**, *44(11)*, 8340-8361.

[6] H. Cheng, B. Meng, C. Li, X. Wang, X. Meng, J. Sunars, *Int. J. Hydrog. Energy.*, **2020**, *45(12)*, 7423-7432.

[7] T. Y. Amiri, K. Ghasemzageh, A. Iulianelli, *Chem Eng Process*, **2020**, *157*, 108148.

[8] S.Sengodan , L. Rong , J. Humphreys , D. Du , W. Xu, H. Wang, S. Tao. *Renew. Sust. Energ. Rev.*, **2018**, *82*, 761-780.

[9] N. Lu, D. Xie, *Int. J. Chem. React. Eng.*, **2016**, *14(1)*, 1-31.

[10] L. Ouyang, K. Chen, J. Jiang, X. S. Yang, M. Zhu, *J. Alloys Compd.*, **2020**, *829*, 154597.

[11] S. S. Mohammadshahi, E. M. Gray, C. J. Webb, *Int. J. Hydrog. Energy.*, **2016**, *41(5)*, 3537-3550.

[12] P. M. Modisha, C. Ouma, R. Garidzirai, P. Wasserscheid, D. Bessarabov, *Energy Fuels*, **2019**, *33(4)*, 2778-2796.

[13] P. T. Aaldto-Saksa, C. Cook, J. Kiviaho, T. Repo, *J.Power Sources*, **2018**, *396*, 803-823.

[14] H. Teng, Q. Pei, C. Ping, *J. Energy Chem.*, **2015**, *24(5)*, 587-594.

[15] M. Aziz, A. T. Wijayanta, A. Nandiyanto, *Energies*, **2020**, *13(12)*, 3062.

[16] A. T. Wijayanta, T. Oda, C. W. Purnomo, T. Kashiwagi, M. Aziz, *Int. J. Hydrog. Energy.*, **2019**, *44(29)*, 15026-15044.

[17] N. Rajalakshmi, T. T. Jayanth, K. S. Dhathathreyan, *Fuel Cells*, **2003**, *3(4)*, 177-180.

[18] I. S. Girnik, Y. I. Aristov, H. Lund, M. J. Kaiser, *Energy*, **2020**, 211.

[19] C. P. Girotto, S. Campos, L. Campos, *Heliyon*, **2020**, *6(2)*, e03397.

[20] G. P. Holland, B. R. Cherry, T. M. Alam, *J. Phys. Chem*, **2004**, *108*, 16420-16426.

[21] B. V. Hassel, J. R. Karra, J. Santana, S. Saita, A. Murray, D. Goberman, *Sep. Purif. Technol.*, **2015**, *142*, 215-226.

[22] P. Sajjan, V. Nayak, M. Padaki, V. Y. Zadorozhnyy, P. A.Konik, *Energy Fuels*, **2020**, *34(9)*, 11699−11707.

[23] A. Alkali, *J. Power Energy Eng.*, **2020**, *8(02)*, 1.

[24] H. Hunter, J. W.Makepeace, T. J. Wood, O. S. Mylius, M.G. Kibble, J. B. Nutter, *J. Power Sources*, **2016**, *329*, 138-147.

[25] S. Liu, T. Chen, Y. Xie, *Int J Green Energy.*, **2020**, *17(4)*, 255-273.

[26] S. A. Grigoriev, A. A. Kalinnikov, N. V. Kuleshov, P. Millet, *Int. J. Hydrog. Energy.*, **2013**, *38(20)*, 8557-8567.

[27] N. Ahmadi, A. D. advand, I. Mirzaei, S. Rezazadeh, *Int. J. Energy Res.*, **2018**, *42(8)*, 2805-2822.

[28] J. X. Liu, H. Guo, F. Ye, C. F. Ma, *Energy*, **2017**, *119*, 299-308.

[29] S. W. Tsai, Y. S. Chen, *Appl. Energy*, **2017**, *188*, 151-159.

[30] B. Wang, K. Wu, Z. Yang, K. Jiao, *Energy Convers. Manag.*, **2018**, *171*, 1463-1475.

[31] S. Yesilyurt, J. B. Siegel, A. G. Stefanopoulou, *J Fuel Cell Sci Technol*, **2012**, *9(2)*.

[32] M. Le Bars, M. G. Worster, *J. Fluid Mech.*, **2006**, *550*, 149-173.

[33] R. J. Kee, M. E. Coltrin, P. Glarborg, *Chemically Reacting Flow: Theory, Modeling, and Simulation*, Wiley, American, **2017**, 91-149.

[34] E. U. Ubong, Z. Shi, X. Wang, *J. Electrochem. Soc.*, **2009**, *156(10)*, B1276.